Robustness Analysis and Experimental Validation of a Fault Detection and Isolation Method for the Modular Multilevel Converter

Shuai Shao, Alan J. Watson, *Member, IEEE*, Jon C. Clare, *Senior Member, IEEE*, and Pat W. Wheeler, *Senior Member, IEEE*

***Abstract*—This paper presents a fault detection and isolation (FDI) method for open-circuit faults of power semiconductor devices in a modular multilevel converter (MMC). The proposed FDI method is simple with only one sliding-mode observer (SMO) equation and requires no additional transducers. The method is based on an SMO for the circulating current in an MMC. An open-circuit fault of power semiconductor device is detected when the observed circulating current diverges from the measured one. A fault is located by employing an assumption-verification process. To improve the robustness of the proposed FDI method, a new technique based on the observer injection term is introduced to estimate the value of the uncertainties and disturbances; this estimated value can be used to compensate the uncertainties and disturbances. As a result, the proposed FDI scheme can detect and locate an open-circuit fault in a power semiconductor device while ignoring parameter uncertainties, measurement error, and other bounded disturbances. The FDI scheme has been implemented in a field-programmable gate array using fixed-point arithmetic and tested on a single-phase MMC prototype. Experimental results under different load conditions show that an open-circuit faulty power semiconductor device in an MMC can be detected and located in less than 50 ms.**

***Index Terms*—Fault detection and isolation (FDI), modular multilevel converter (MMC), sliding-mode observer (SMO).**

I. Introduction

The modular multilevel converter (MMC) is the state of the art in multilevel converters and is receiving great interest both from academia and industry. It has a number of desirable features such as modular configuration, low harmonic distortion, low-voltage stress on the semiconductor devices, high-voltage and high-power capability, and simple realization of redundancy [1]. In addition, the cells of an MMC are fed by capacitors and no multiphase transformers are required. A comprehensive introduction of the operation of the MMC is given in [2]. The review paper [3] summarizes the latest achievements regarding the MMC in terms of modeling, control, modulation, applications, and future trend.

Manuscript received October 8, 2014; revised March 27, 2015, January 19, 2015, and June 10, 2015; accepted July 22, 2015. Date of publication July 29, 2015; date of current version December 10, 2015. Recommended for publication by Associate Editor A. Perez.

The authors are with the Power Electronics, Machines and Control Group, School of Electrical and Electronic Engineering, The University of Nottingham, Nottingham NG7 2RD, U.K. (e-mail: eexss21@nottingham.ac.uk; Alan.watson@nottingham.ac.uk; Jon.Clare@nottingham.ac.uk; Pat.Wheeler@nottingham.ac.uk).

Color versions of one or more of the figures in this paper are available online at http://ieeexplore.ieee.org.

Digital Object Identifier 10.1109/TPEL.2015.2462717

Power semiconductor switches are among the most failure-prone components in a power converter and each of these devices is a potential failure point [4]. With large numbers of semiconductor devices, the possibility of fault occurrence is much larger than for normal two-level voltage-source converters (VSCs). Faults in power semiconductor devices cause a power converter operating far away from its setting point and this abnormal operation cannot be overcome by a feedback controller. If the faulty operation is allowed, other devices may be damaged and a shutdown of the plant may follow. Therefore, it is vital to detect and isolate these faults immediately after their occurrence.

Fault detection and isolation (FDI) deals with detecting anomalous situations [fault detection (FD)] and addressing their causes (fault isolation, FI) [5]. An FDI scheme can be implemented either by hardware method or analytical (software) method [5], [6]. Hardware FDI employs repeated components or additional sensors, and a fault can be obtained if the behavior of the process components is different from the redundant ones, or the additional sensors detect anomalous signals. It is straightforward and reliable but increases the cost, size, and hardware complexity of the plant. The basic idea of analytical FDI is to check the consistency between the actual system behavior and its estimated behavior [7]. The estimated behavior can be obtained either from a mathematical model of the system (for example, using observers) or an analysis of the historical data (for example, using data mining or neural networks). Although the algorithm is more sophisticated, the cost and hardware complexity of employing the analytical method is less than that for the hardware method. The application of the analytical FDI methods is boosted by the great advances of the computer technology in recent decades [6].

There are two types of faults seen in a fully controlled power semiconductor device: short-circuit fault (remains ON regardless of the gate signal) and open-circuit fault (remains OFF regardless of the gate signal). Any short-circuit fault needs to be detected within $10\,\mu$s to save the semiconductor devices from destruction and to avoid a shoot-through fault with the complementary device [8]. A short circuit in an insulated-gate bipolar transistor (IGBT) is usually detected using a hardware circuit, often with additional sensors and associate circuits. These sensors and circuits are usually integrated in a gate driver to form an active/smart gate driver [9], [10]. The additional sensors and circuits add extra cost and size to the system. Furthermore, these active gate drivers can fail themselves due to their complexity and hence decrease the reliability of the power converter.

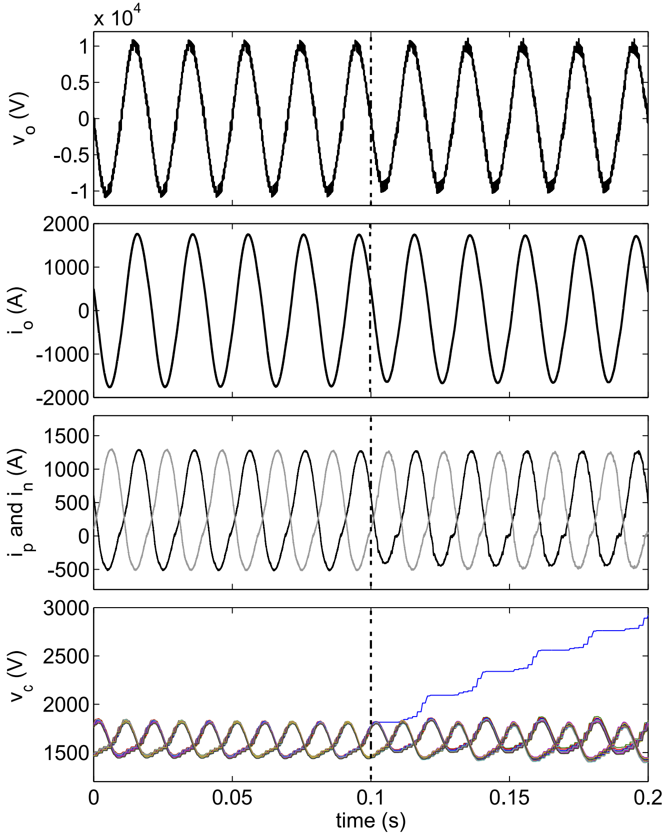

Fig. 1. Simulation results of an MMC with parameters same as an industrial 24-MW MMC and an open-circuit fault occurs at 0.1 s: from top to bottom, output voltage (v_o), output current (i_o), arm currents (i_p and i_n), and capacitor voltages (v_c).

This paper deals with detection and isolation of an open-circuit faulty switch in an MMC. The typical characteristics of an MMC in the event of an open-circuit fault in a power device is shown in Fig. 1, where the parameters are same as an industrial 24-MW MMC [11] and an open-circuit fault occurred at 0.1 s. Only one of the phases is considered. It can be seen that an open-circuit fault is not fatal immediately to an MMC; however, the fault needs to be detected and removed within 0.1 s to avoid secondary damages on other devices. The cause of an open-circuit fault can be various: lifting/fusing of bonding wires, a driver failure, or a communication problem between the controller and driver. The gate driver is recognized as the third most failure prone components according to an industry-based survey [12]. The simplest detection method is to use an active gate driver as mentioned previously. Analytical redundancy can be used to detect an open-circuit fault as this type of fault is not fatal immediately and can be tolerated by the power converter for some time [13]. Several analytical FDI methods based on the analysis of the output voltage waveform are reported. In [14], a faulty cell in a flying capacitor converter is detected and localized by analyzing the switching frequency of the output phase voltage. This technique has also been applied to a cascaded H-bridge [15] where an open- or short-circuit fault can be detected. In [16], the characteristics of the output phase voltage are analyzed in the time domain, and the occurrence of a fault is detected by the degradation of the output voltage, while the fault is located by comparing the output phase voltage with all the possible phase fault voltages. In [17], an artificial intelligence FDI algorithm is proposed, where the historical data of the output phase voltages both in normal and faulty conditions are used to train a neural network. Survey [18] has presented a comprehensive review of the reliability of power electronics systems including methodologies of assessing reliability, methods to detect and locate faults as well as fault tolerate operation. Survey [19] has summarized the recent fault tolerance techniques for three-phase VSCs.

A sliding-mode observer (SMO)-based FDI technique for an MMC was proposed in [20] and [21], where a faulty power semiconductor device can be detected and located within 100 ms. The work presented in this paper is an improved method. This method is simpler using only one SMO equation and can detect and locate an open-circuit fault in less than 50 ms. Furthermore, a technique is proposed to compensate for any parameter uncertainties, measurement errors, and other bounded disturbances. The resultant FDI scheme can detect an open-circuit faulty power semiconductor device while rejecting any uncertainties and disturbances. The practical implementation of the SMO-based FDI scheme in a field-programmable gate array (FPGA) is also discussed in this paper and the experimental results at different load conditions are presented.

II. Sliding-Mode Observer

A. Introduction

An observer is a mathematical replica of a system to estimate its internal states, driven by the input of the system and a signal representing the discrepancy between the estimated and actual states [22]. In the earliest observers such as the Luenberger observer, the differences between the estimated outputs and the actual outputs of the plant are fed back to the observer linearly, and the estimated states cannot converge to the measured states in the presence of a disturbance [22], [23]. The SMO employs a high-gain switching function of the discrepancy between the estimated and actual outputs to force the estimated states to the actual states asymptotically.

A first-order system (1) is used in this paper

$$\dot{x} = ax + u. \tag{1}$$

An SMO for (1) is introduced

$$\dot{\hat{x}} = a\hat{x} + bu + L\text{sgn}(x - \hat{x}) \tag{2}$$

$$\text{sgn}(x) = \begin{cases} 1, & x > 0 \\ 0, & x = 0 \\ -1, & x < 0 \end{cases} \tag{3}$$

where $\hat{x}$ donates the estimated/observed state of x and L denotes the observer gains designed to drive $\hat{x} \to x$ in finite time. Subtracting (2) from (1) yields the dynamic error between the observed and measured states

$$\dot{\tilde{x}} = a\tilde{x} - L\text{sgn}(\tilde{x}), \tilde{x} \triangleq x - \hat{x}. \tag{4}$$

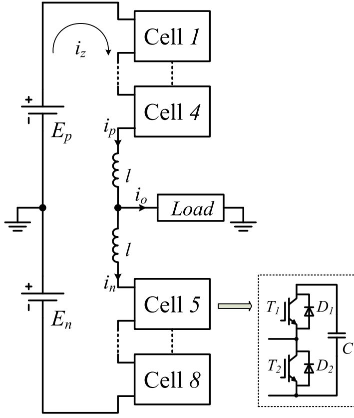

Fig. 2. Single-phase eight-cell MMC converter used for simulation.

TABLE I
CIRCUIT PARAMETERS USED IN THE SIMULATION

DC voltage	$E_p + E_n$	6000 V
Average circulating current	I_z	120 A
Nominal voltage of the cell capacitors	V_c	1500 V
Capacitance of cell capacitors	C	4 mF
Inductance of the arm inductors	l	3 mH
Load		$5\,\Omega$, 4 mH

Choosing $L > |a\tilde{x}|$, we obtain

$$\tilde{x}\dot{\tilde{x}} = \tilde{x}(a\tilde{x} - L\text{sgn}(\tilde{x})) = |\tilde{x}|(|a\tilde{x}| - L) < 0 \tag{5}$$

which will force $\tilde{x}$ and $\dot{\tilde{x}}$ to zero and keep zero thereafter, this motion along a line is the so-called *sliding mode* [24].

B. SMO for an MMC

An SMO can be built for an MMC based on (2). In this paper a single-phase eight-cell MMC is considered; nevertheless, the method is versatile and can be used for MMC with hundreds of cells.

The circuit diagram and parameters of the MMC used for the analysis and simulation are presented in Fig. 2 and Table I, respectively. T_1 and T_2 in Fig. 2 represent the upper and lower power semiconductor devices in a cell.

According to the Kirchhoff's voltage law, we obtain the following equation for the MMC (see Fig. 2):

$$l\frac{di_p}{dt} + l\frac{di_n}{dt} = -\sum_{i=1}^{8} S_i v_{ci} + E_p + E_n \tag{6}$$

where i_p and i_n are the upper and lower arm currents, l is the inductance of arm inductors, E_p and E_n are the dc voltages, and v_{ci} and S_i are the capacitor voltage and switching state of the cell i, respectively. S_i is defined in Table II, where g_1 and g_2 are the gate signals for the upper and lower switch in a cell.

Since the circulating current of the MMC converter is $i_z = (i_p + i_n)/2$ [25], (6) can be rewritten as

$$2l\frac{di_z}{dt} = -\sum_{i=1}^{8} S_i v_{ci} + E_p + E_n. \tag{7}$$

TABLE II
SWITCHING STATE S IN NORMAL CONDITIONS

S	Driving signals
1	$g_1 = 1, g_2 = 0$
0	$g_1 = 0, g_2 = 1$

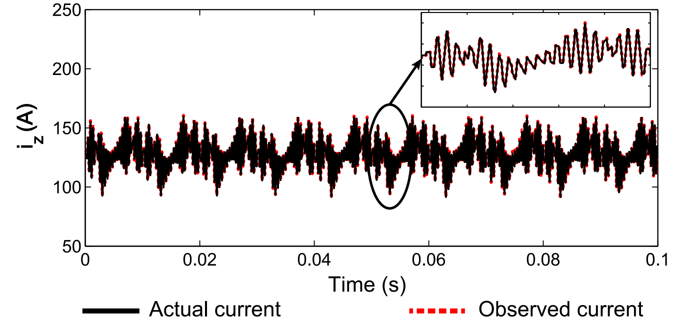

Fig. 3. Simulation waveforms of i_z and $\hat{i}_z$ when the MMC is fault free.

Based on (2) and (7), an SMO can be obtained for the MMC

$$\frac{d\hat{i}_z}{dt} = -\frac{1}{2l}\left(\sum_{i=1}^{8} S_i v_{ci} - E_p - E_n\right) + L\text{sat}\left(i_z - \hat{i}_z\right). \tag{8}$$

It is noted that a saturation function sat(x) (9) is utilized instead of sgn(x) for less chattering of the observed states according to [26]

$$\text{sat}(x) = \begin{cases} 1, & x \geq h \\ x/h, & -\text{h} < x < h,\ h > 0 \\ -1, & x \leq -h \end{cases} \tag{9}$$

where h is a constant.

A simulation has been carried out in SIMULINK/PLECS to verify the SMO (8). The parameters of the MMC are listed in Table I and the observer gain L is 6×10^4 and $h = 1$. Fig. 3 shows the simulation results where it can be seen that $\hat{i}_z$ follows i_z closely.

III. FAULT DETECTION AND ISOLATION USING SMO

A. Mathematical Basis

The *FD* is first considered and a fault is added to the first-order system

$$\dot{x} = ax + bu + kf \tag{10}$$

where f represents the value of the fault and k the corresponding coefficients. It is noted that f is often a very large value and cannot be overcome by the feedback control.

The difference between the observed and measured states can be obtained by subtracting (10) from (2)

$$\dot{\tilde{x}} = a\tilde{x} + kf - L\text{sgn}(\tilde{x}). \tag{11}$$

If we choose

$$L < |kf| \tag{12}$$

then at the faulty condition $\tilde{x}_1\dot{\tilde{x}}_1 > 0$, the observer cannot enter the sliding mode and $\hat{x}$ will diverge from x significantly. For an open-circuit fault at cell i in the MMC, $f = v_{ci}/(2l), k_i = 1$, and therefore, L needs to satisfy the following condition to detect an open-circuit faulty switch:

$$L < v_{ci}/2l. \tag{13}$$

The occurrence of a fault can be detected by comparing $|x - \hat{x}|$ with a given threshold value.

For the *FI*, an assumption-verification method was proposed [20], [21]. The procedure is to assume a location for the fault, modify the observer equation accordingly, and to again compare the observed states with the measured states. $\hat{x}$ will converge to x if the assumption is correct. In this case, kf is included in the observer as well

$$\dot{\hat{x}} = a\hat{x} + bu + kf + L\text{sgn}(x - \hat{x}). \tag{14}$$

Subtracting (14) from (10) yields the dynamical error

$$\dot{\tilde{x}} = a\tilde{x} - L\text{sgn}(\tilde{x}) \tag{15}$$

which is the same as (4), where sliding condition $\tilde{x}\dot{\tilde{x}} < 0$ is satisfied and $\hat{x} \to x$ in finite time. On the other hand, if the assumed fault location is incorrect, $\hat{x}$ will keep diverging from x. In this way, the fault can be located.

B. Flowchart

The flowchart of this algorithm is shown in Fig. 4. There are two modes in this algorithm: FD mode and FI mode.

FD mode: This mode monitors whether a fault occurs. If the difference between the observed and measured circulating current $|i_z - \hat{i}_z|$ is larger than a threshold value I_{th1} and this condition persists for 0.4 ms, then an open-circuit fault occurs and the FDI scheme enters FI mode; otherwise, the FDI scheme stays in FD mode.

FI mode: This mode locates where is the open-circuit fault. The assumption-verification process is employed. The cell i, T_j is assumed to be the faulty device, the switching state S_i in SMO (8) is modified according to Table II in [20]. If cell i, T_j is the actual faulty device, $\hat{i}_z$ converges to i_z; otherwise, $\hat{i}_z$ diverges from i_z. It is important to note that during some points in the faulty period, the current of the faulty arm can be clamped to zero because of the fault, and the converter is unobservable in these moments. Therefore, $\hat{i}_z$ is set to $\hat{i}_z = i_z$ when the current of the assumed faulty arm is 0 as shown in Fig. 4.

It is noted that the threshold values I_{th1} and I_{th2} are load dependent. In the case of faulty power semiconductor device, $\hat{i}_z$ diverges from i_z slower under light load than that under heavy load. The divergence rate between $\hat{i}_z$ and i_z is also related to the observer gain L according to (11). There are many choices for I_{th1} and I_{th2} and, for example, one of them can be

$$\begin{cases} L = \dfrac{I_z}{I_{zo}} L_o, & L \geq \dfrac{L_o}{8} \\ I_{\text{th1}} = 2I_z, & I_{\text{th1}} \geq \dfrac{I_{zo}}{2} \\ I_{\text{th2}} = I_z, & I_{\text{th2}} \geq \dfrac{I_{zo}}{4} \end{cases} \tag{16}$$

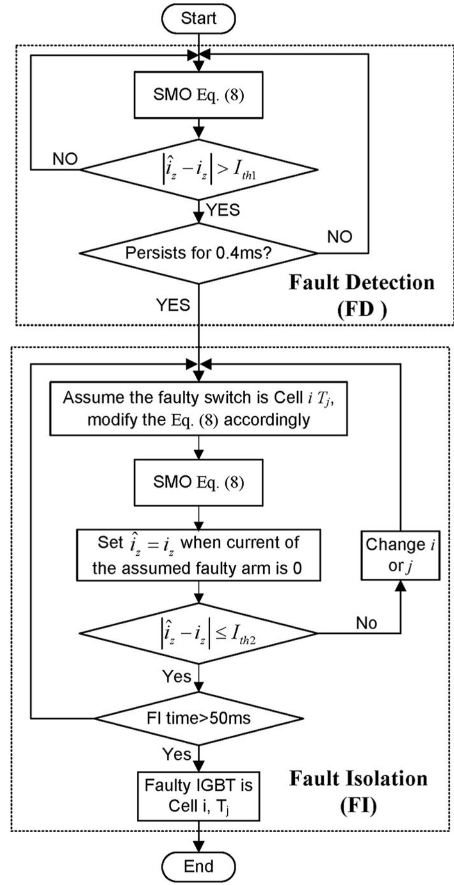

Fig. 4. Flowchart of the FDI method for an MMC.

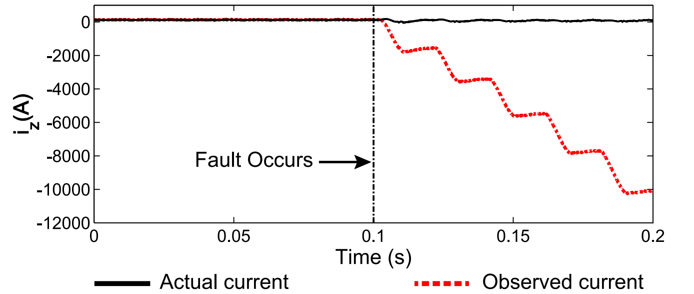

Fig. 5. Simulation waveforms of i_z and $\hat{i}_z$ when an open-circuit fault occurs at cell $1, T_1$ at 0.1 s.

where L_o denotes the observer gain under the full load, I_z the circulating current, and I_{zo} the circulating current under full load. As shown in (16), it is recommended that L, I_{th1}, and I_{th2} are larger than certain values to reject the parameter uncertainties and measurement noise.

Simulations have been carried out to verify the proposed algorithm with the parameters listed in Table I. L needs to satisfy $L < V_c/2l = 2.5 \times 10^5$ according to (12), and L is set to 6×10^4 so that an open-circuit fault can be detected and located within 50 ms.

In Figs. 5–7, an open-circuit fault occurs at cell $1, T_1$ at 0.1 s. In Fig. 5, no FDI scheme is applied and $\hat{i}_z$ diverges from i_z at a very high rate after the occurrence of the fault. In Figs. 6 and 7,

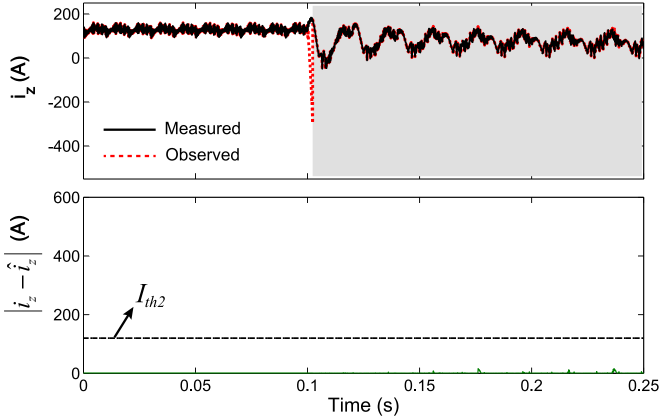

Fig. 6. Simulation results of FDI: the open-circuit fault occurs at cell $1, T_1$ and the assumed faulty switch is cell $1, T_1$.

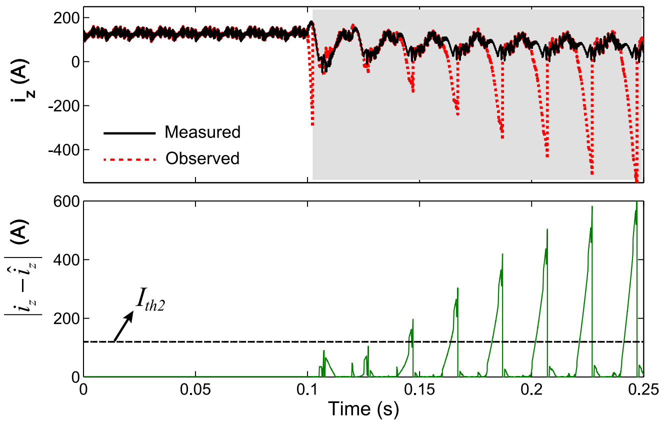

Fig. 7. Simulation results of FDI: the open-circuit fault occurs at cell $1, T_1$ and the assumed faulty switch is cell $2, T_1$.

the FDI algorithm enters FI mode once $|i_z - \hat{i}_z| > I_{\text{th1}}$ persists for 0.4 ms. The FI mode is indicated with a grey background. In Fig. 6, the assumed faulty switch is the actual one and $\hat{i}_z$ converges to i_z in FI mode; in Fig. 7, the assumed faulty switch is cell2, T_1, which is not the actual faulty device; $\hat{i}_z$ diverges from i_z in FI mode and $|\hat{i}_z - i_z| > I_{\text{th2}}$ in 50 ms.

IV. Robustness Analysis and Disturbance Compensation

In any analytical FDI scheme, certain assumptions including accurate physical parameters, precise measurements, and linear time-invariant operation are made when modeling a plant [5]. However, these assumptions may not be accurate. The parameters may contain uncertainties, for example, the parasitic resistance of an inductor, and may degrade over time. Measurements usually have errors superimposed on the signals. These errors can include electronic white noise and incorrect scaling factors between the measured and actual variable. Furthermore, all dynamical plants are nonlinear, but behave almost linearly. These uncertainties and disturbances may lead to divergence between the actual system behavior and its estimated behavior, giving false alarms. The robustness of an FDI scheme is the degree to which the system can maximize the sensitivity of the detection of actual malfunctions while discriminating between apparent faults and disturbances due to measurement noise, parameter uncertainty, or transients [5].

The desirable features of this FDI method are as follows:

1) white noise in the measurement does not affect the observed states, so it does not affect the FDI;
2) the value of the parameter uncertainties, scaling errors in the measurements, and other bounded disturbance is estimated using the observer injection term; this estimated value is used to compensate for the uncertainties and disturbances.

In summary, the proposed method is able to detect and locate an open-circuit fault of a power semiconductor device while ignoring parameter uncertainties, measurement noise, or other bounded disturbances. This desirable feature will be discussed in this section.

A. Mathematical Basis

The first-order system (1) and its SMO (2) are considered to demonstrate the features described above. By adding the uncertainties and disturbances to (2), we obtain

$$\dot{\hat{x}} = (a + \Delta a)\hat{x} + (b + \Delta b)(u + \Delta u) + d + L\text{sgn}(x - \hat{x}) \tag{17}$$

where Δa and Δb denote the values of parameter uncertainties, and Δu the value of the measurement noise consisting of white noise Δr and a scaling error between the measured and actual variable Δs. It is assumed that the values of these uncertainties and disturbances are bounded and are smaller than the value of a fault.

Subtracting (17) from (1), we obtain the errors between the measured and observed states

$$\dot{\tilde{x}} = a\tilde{x} - \overbrace{(\Delta a\hat{x} + \Delta b(u + \Delta u) + b_1\Delta u + d_1)}^{D} - L\text{sgn}(\tilde{x}). \tag{18}$$

If we choose L satisfying

$$L > |a\tilde{x}| + |D| \tag{19}$$

then $\tilde{x}\dot{\tilde{x}} < |\tilde{x}|(|a\tilde{x}| + |D| - L) < 0$; the sliding mode in (18) occurs and $\tilde{x} \to 0$ (namely $\hat{x} \to x$) in finite time. $\hat{x}$ is not affected by the uncertainties or the disturbances.

Based on (12) and (19), the observer gain needs to satisfy the following condition to discriminate an open-circuit fault from uncertainties and disturbances:

$$|a\tilde{x}| + |D| < L < |kf|. \tag{20}$$

Two simulations have been carried out to verify the above analysis. In these simulations the parameter uncertainties and measurement noise are added to the observer; all other conditions are the same as for Figs. 6 and 7. An open-circuit fault in cell $1, T_1$ occurred at 0.1 s and in FI mode the assumed faulty switch is the actual one. In the first simulation (see Fig. 8), 5% white noise is added to all the measurements as shown in (21). In the second simulation (see Fig. 9), parameter uncertainties

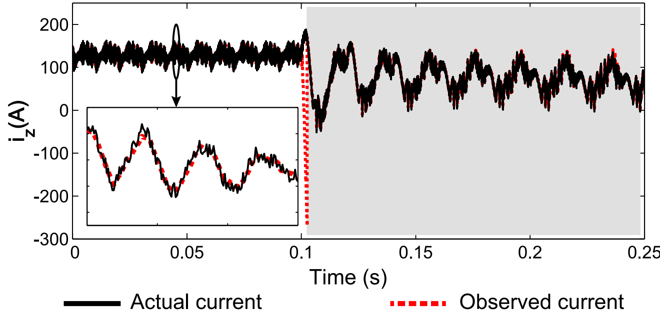

Fig. 8. Simulation results of $\hat{i}_z$ and i_z with 5% white noise on the measurement.

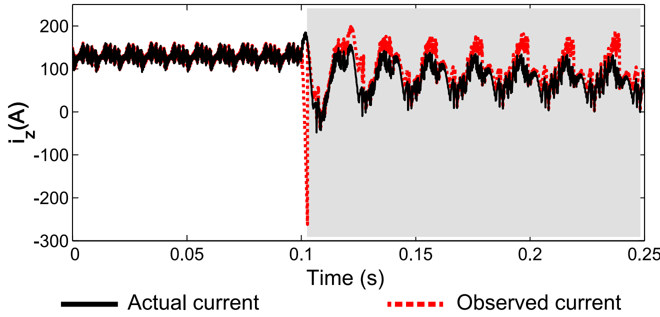

Fig. 9. Simulation results of $\hat{i}_z$ and i_z with parameter uncertainties and systematic measured error.

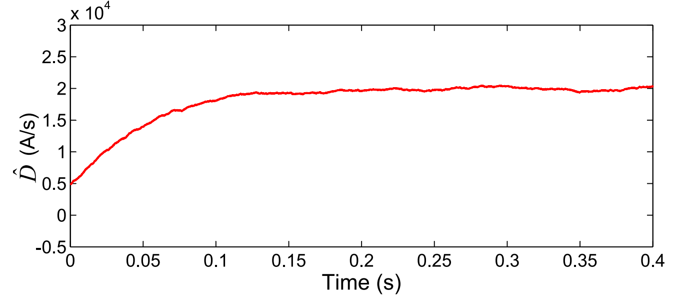

Fig. 10. Simulation results of $\hat{D}$ (estimated value of the uncertainties and disturbances).

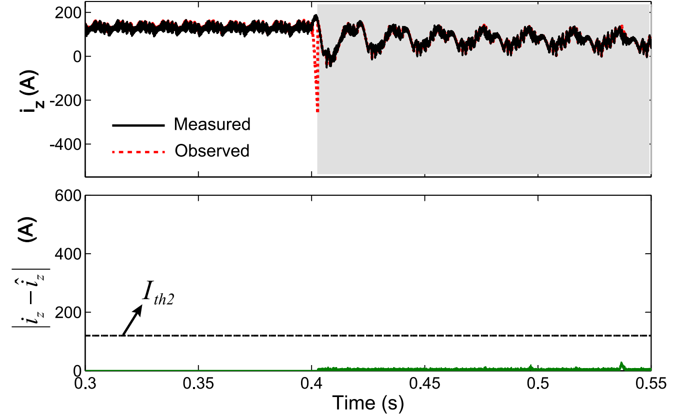

Fig. 11. Simulation results of FDI with uncertainties and disturbances: open-circuit fault at cell $1, T_1$ and assumed faulty device at cell $1, T_1$.

and 1% scaling errors in measurements are added to the SMO as shown in (22)

$$\begin{cases} i_{z(mes)} = (1 + 5\% r_1) i_z \\ v_{ci(mes)} = (1 + 5\% r_2) v_{ci} \\ e_{p,n(me)s} = (1 + 5\% r_2) e_{p,n} \end{cases} \tag{21}$$

$$\begin{cases} \hat{l} = (1 + 0.1) l \\ R_l = 0.05\,\Omega \\ i_{z(mes)} = (1 + 0.01) i_z \\ v_{ci(mes)} = (1 - 0.01) v_{ci} \\ e_{p,n(mes)} = (1 + 0.01) e_{p,n} \end{cases} \tag{22}$$

where the subscript mes denotes measured variables; r_1, r_2, and r_3 are random numbers ranging from -1 to 1 and change at every calculation cycle; $\hat{l}$ denotes the inductance used in the observer; and R_l denotes the parasitic resistance of the arm inductors.

In the fault-free condition, it can be seen in Figs. 8 and 9 that $\hat{i}_z$ converge to i_z and is not affected by the uncertainties and disturbances. It can also be seen in Fig. 8 that white noise in the measurements does not affect the FI which is indicated with gray background. Since the average value of the white noise is zero, its effect on the observer is self-canceling, and therefore, the observer and FDI scheme are not affected. However, parameter uncertainties and scaling errors in the measurements will lead to incorrect FI. As shown in Fig. 9, there is noticeable difference between the $\hat{i}_z$ and i_z. Larger observer gain and threshold values can be used to alleviate the incorrect FI, but more time will be needed to detect and locate a fault.

B. Compensation of Uncertainties and Disturbances

In this section, the value of parameter uncertainties, scaling errors in the measurements, and other bounded disturbances are estimated, and this estimated value is used to compensate the observer to achieve robust FDI.

Once (18) enters the sliding mode, $\tilde{x} \to 0$ and $\dot{\tilde{x}} \to 0$, and it can be obtained that

$$D = -L\mathrm{sgn}(\tilde{x}). \tag{23}$$

When the MMC is fault free (0 to 0.1 s in Figs. 8 and 9), the uncertainties and disturbances D are counterbalanced by the observer injection term $-L\mathrm{sgn}(\tilde{x})$ according to (23). Therefore, the value of D can be extracted from $-L\mathrm{sgn}(\tilde{x})$. Since $-L\mathrm{sgn}(\tilde{x})$ is a high-frequency switching term, a low-pass filter is applied to obtain the estimated value of D

$$\hat{D} = \frac{-L\mathrm{sgn}(\tilde{x})}{1 + \tau s} \tag{24}$$

where $\hat{D}$ denotes the estimated value of the uncertainties and disturbances, and τ denotes time constant of the low-pass filter. A simulation has been undertaken with the white noise (21), scaling errors, and parameter uncertainties (22), and the simulation results are shown in Fig. 10. The value of $\hat{D}$ is about

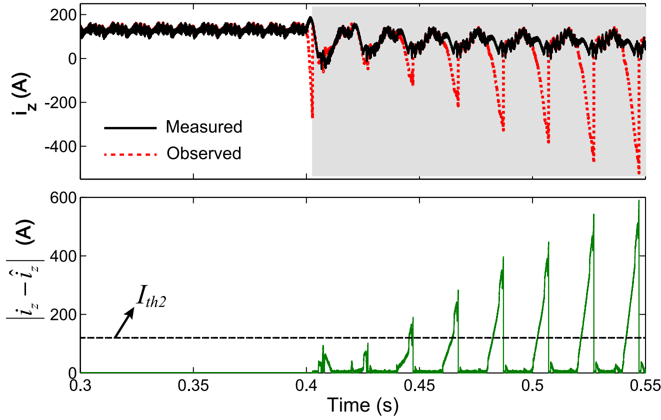

Fig. 12. Simulation results of FDI with uncertainties and disturbances: open-circuit fault at cell $1, T_1$ and assumed faulty device at cell $2, T_1$.

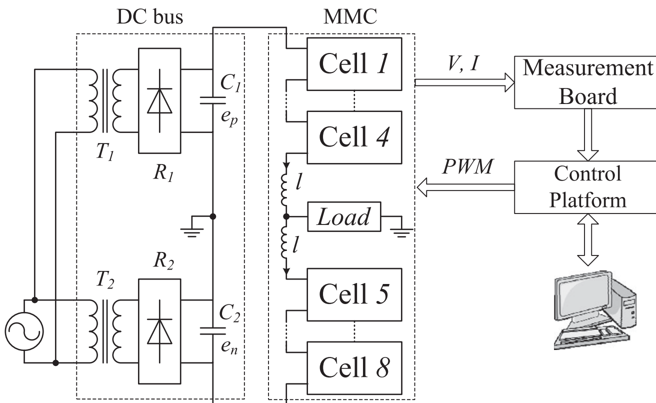

Fig. 13. Diagram of the experimental MMC rig.

20 000 A/s and is caused by the parameter uncertainties and scaling errors in the measurements (the effect of the white noise is self-canceling). Because of the uncertainties and disturbances, the observer injection term $L\text{sgn}(\tilde{i}_z)$ operates at a biased condition with an offset of 20 000 A/s; as a result, the observer becomes sensitive to noise and incorrect FI is caused. In order to achieve robust FDI, $\hat{D}$ is added to SMO to compensate for the uncertainties and disturbances

$$\frac{d\hat{i}_z}{dt} = -\frac{1}{2l}\left(\sum_{i=1}^{8} S_i v_{ci} - E_p - E_n\right) + L\text{sat}\left(i_z - \hat{i}_z\right) - \hat{D}. \tag{25}$$

It is noted that $\hat{D}$ only updates when the system is fault free.

Simulations have been carried out to test the FDI with compensation of the uncertainties and disturbances. The white noise [condition (21)], parameter uncertainties and scaling errors in measurements [condition (22)] are considered. $\hat{D}$ is added to compensate for the uncertainties and disturbances. Simulation results are shown in Figs. 11 and 12. It can be seen in Figs. 11 and 12 that the uncertainties and disturbances are compensated and the open-circuit fault can be detected and located without influenced by the uncertainties and disturbances.

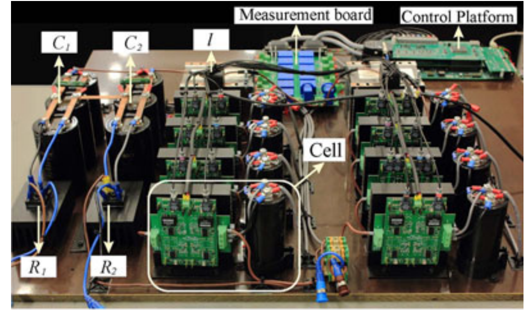

Fig. 14. Photograph of the experimental rig.

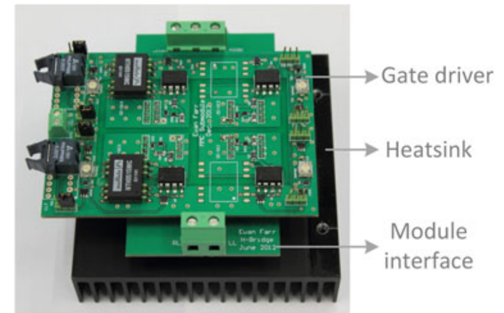

Fig. 15. Photograph of the assembled power module with gate driver and heat sink.

TABLE III
CIRCUIT PARAMETERS USED IN THE EXPERIMENTS

Rated power	P	2.5 kW
Average circulating current	I_z	5.2 A
Nominal voltage of the cell capacitors	V_c	120 V
Capacitance of cell capacitors	C	1.5 mF
Inductance of the Arm inductors	l	2.6 mH
IGBT modules		F4-50R06W1E3
Voltage transducer		LEM LV 25-P
Current transducer		LEM LA 55-P
DSP		TMS320C6713
FPGA		Actel A3P1000

V. EXPERIMENTAL VALIDATION OF THE FDI METHOD

An MMC experimental rig has been built to validate the FDI method. The method is implemented in an FPGA using fixed-point arithmetic. The implementation procedures and experimental results are presented in this section.

A. Experimental Rig

The diagram and a photograph of the laboratory setup are shown in Figs. 13 and 14, respectively. The assembled power module with gate driver and heat sink is shown in Fig. 15. The power module is soldered to a module interface board and attached to a heat sink. The cell capacitances are selected such that the ripple of the capacitor voltages is less than 10% [27] and arm inductances are chosen such that the switching harmonic is less than 60% of the nominal circulating current. The parameters of the experimental rig are listed in Table III.

The control scheme of the MMC experimental rig is shown in Fig. 16. The subscripts p and n denote the upper and lower

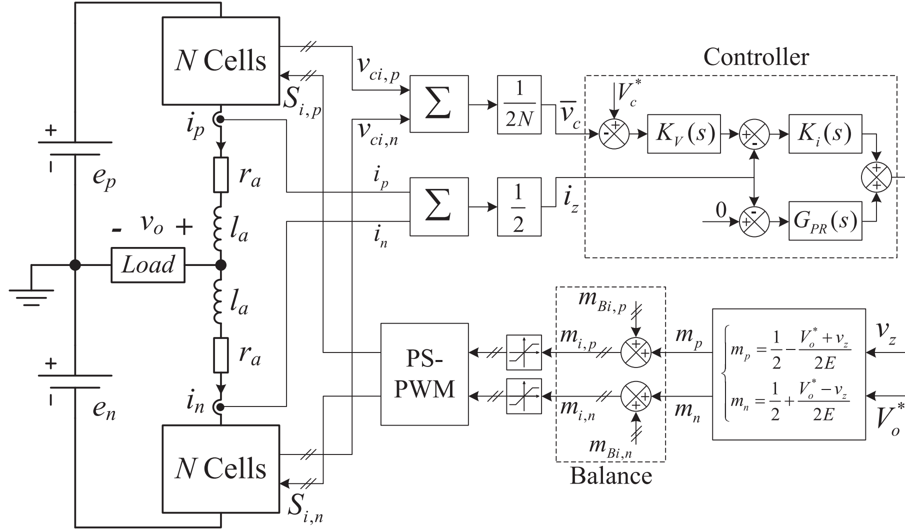

Fig. 16. Control scheme of the MMC experimental rig.

TABLE IV
DETAILS OF THE COMPENSATORS

$K_i(s)$	$k_{p1} + \frac{k_{i1}}{s}$	$k_{p1} = 6.3, k_{i1} = 500$
$K_v(s)$	$k_{p2} + \frac{k_{i2}}{s}$	$k_{p2} = 0.66, k_{i2} = 74$
$G_{PR}(s)$	$k_{p3} + \frac{2k_{i3}\omega_c s}{s^2+2\omega_c s+\omega_o^2}$	$k_{p3} = 0.1, k_{i3} = 80$
		$\omega_c = 5, \omega_o = 200\pi$

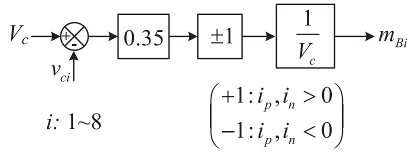

Fig. 17. Block diagram of the capacitor voltage balancing [28].

arms, respectively. $K_v(s)$ and $K_i(s)$ are the PI compensators for the regulation of the average capacitor voltages; $G_{\mathrm{PR}}(s)$ is a proportional resonant (PR) compensator to suppress the second harmonic of the MMC circulating current. The details of these compensators are listed in Table IV. v_z is the output of these compensators and V_o^* is the command for the ac voltage. Modulation indices for the upper and lower arms m_p and m_n can be obtained with v_z and V_o^*. m_{Bi} is the term for balancing the capacitor voltages and can be obtained using block diagram shown in Fig. 17. $m_{i,p}$ and $m_{i,n}$ are the modulation indices for cell i in the upper and lower arms, respectively. The phase-shifted PWM is used to generate gate signals for the IGBTs.

B. FPGA Implementation of the SMO

The SMO is implemented in the FPGA to obtain the quasi-analog behavior of the observed states. The observer is implemented using fixed point as there is no floating point unit in the A3P1000 FPGA. The implementation includes three steps.

Step 1: Convert the analog observer into discrete form. Using $\dot{x}_i[k] = (x_i[k+1] - x_i[k])/T_s$, the discrete SMO (8) can be expressed as

$$\hat{i}_z[k+1] = \hat{i}_z[k] - \frac{T_s}{2l}\left(\sum_{i=1}^{8} S_i \hat{v}_{ci}[k] - e_p[k] - e_n[k]\right) + T_s L\mathrm{sat}\left(\tilde{i}_z[k]\right). \tag{26}$$

Step 2: Scale the actual variables $i_z[k], v_{ci}[k], e_{p,n}[k]$ in (26) to the digital variables $I_z[k], V_{ci}[k], E_{p,n}[k]$ sensed by the A/D converters. The relationships between values of actual variables and the values of the corresponding digital variables are

$$\begin{cases} i_z[k] = m_I I_z[k] \\ v_{ci}[k] = m_V V_{ci}[k], \quad i = 1, \ldots, 8 \\ e_p[k] = m_E E_p[k], \quad e_n[k] = m_E E_n[k] \end{cases} \tag{27}$$

where m_I, m_V, and m_E are the scaling factors.

Substituting (27) into (26), we obtain

$$\hat{i}_z[k+1] = \hat{i}_z[k] - \overbrace{\frac{m_V T_s}{2m_I l}\left(\sum_{i=1}^{8} S_i V_{ci}[k]\right)}^{\text{Term1}} + \overbrace{\frac{m_E T_s}{2m_I l}\left(E_p[k] + E_n[k]\right)}^{\text{Term2}} + \overbrace{\frac{LT_s}{m_I}\mathrm{sat}\left(m_I \tilde{i}_z[k]\right)}^{\text{Term3}}. \tag{28}$$

Step 3: Convert the parameters from floating point to fixed point and implement the observer in the FPGA using *Verilog*. The observer equations are break down into three parts as shown in (28). The block diagram of FPGA program is illustrated in Fig. 18. The subtraction is performed by adding the complement of the subtracted number and the multiplication is carried out by shifting.

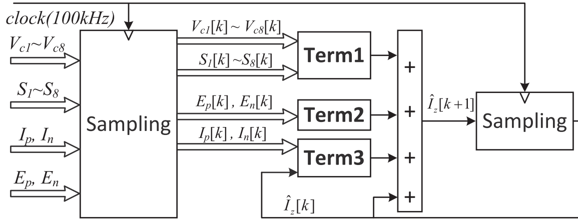

Fig. 18. Block diagram of the experimental implementation of the SMO.

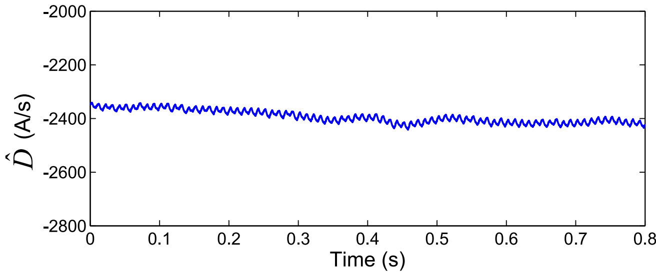

Fig. 19. Experimental results of $\hat{D}$ (estimated uncertainties and disturbances).

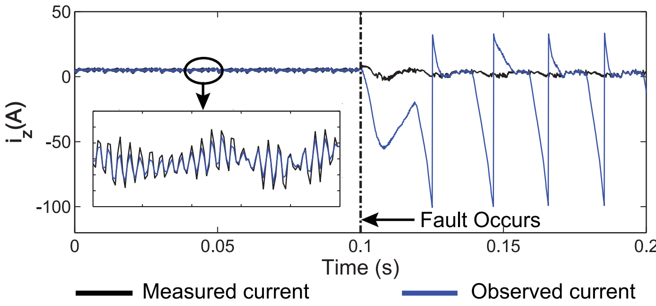

Fig. 20. Experimental results of i_z and $\hat{i}_z$ when an open-circuit fault occurs at an IGBT at 0.1 s.

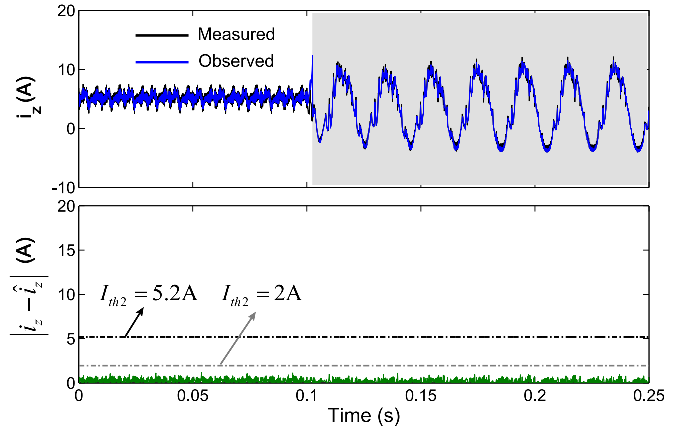

Fig. 21. Experimental results of the FDI: an open-circuit fault occurs at cell $6, T_2$ and the assumed faulty device is cell $6, T_2$.

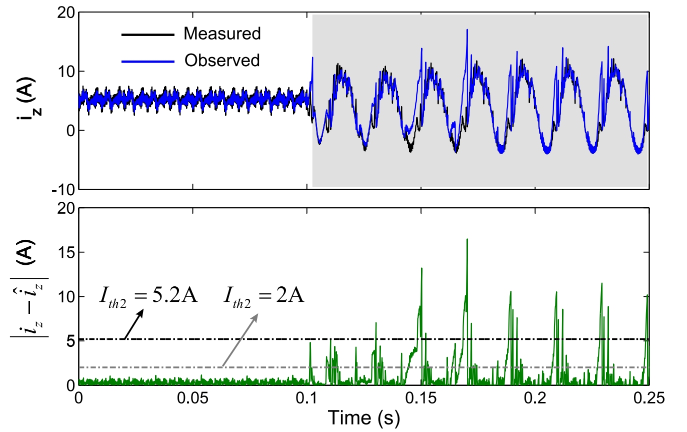

Fig. 22. Experimental results of the FDI: an open-circuit fault occurs at cell $6, T_2$, while the assumed faulty device is cell $7, T_2$.

C. Experimental Results

In the experimental tests, to create the open-circuit fault condition on a power semiconductor device, the gate drive signal of the device is set to low. The experimental results are taken using a C6713 host-port interface daughtercard and the waveforms are shown in Figs. 19–26. In the experimental results shown in Figs. 19–22, the MMC rig operates under full-load condition with a circulating current $I_{zo} = 5.2$ A. The observer gain L needs to satisfy condition (13): $L < V_c/(2l) = 2.5 \times 10^4$ and 1.2×10^4 is chosen for L and $h = 0.25$.

In these experimental tests, parameter uncertainties and measurement noise are considered: 10% error in the inductance l, 0.11-Ω parasitic resistance in the arm inductors, and 5% scaling error in the measurement of the e_p. A low-pass filter with a time constant of 0.1 s is used to filter the switching frequency of $-L\text{sgn}(\tilde{x})$ as shown in (24). This filter is implemented in the DSP. The estimated value of the uncertainties and disturbances is about -2400 A/s, as shown Fig. 19. This estimated value is put into the observer to compensate for the uncertainties and disturbances. In the experimental results in Fig. 20–26, this compensation has been added.

Fig. 20 shows experimental waveforms of the fault occurrence. An open-circuit fault occurs at cell $6, T_1$ occurs at 0.1 s, no FDI algorithm is applied here. Before the fault, $\hat{i}_z$ follows i_z closely; after the fault occurrence, $\hat{i}_z$ diverges from i_z significantly.

Figs. 21 and 22 show waveforms with different assumed fault locations. In these two figures, an open-circuit fault occurs cell $6, T_2$ at 0.1 s. At full load, the circulating current is 5.2 A and the threshold values for FDI are chosen as $I_{\text{th1}} = 10.4$ A, $I_{\text{th2}} = 5.2$ A according to (16). $I_{\text{th2}} = 5.2$ A is indicated using a black dash line. In Fig. 21, the assumed faulty switch is the actual one—cell $6, T_2$, $\hat{i}_z$ converge to i_z; in Fig. 22, the assumed faulty switch is cell $7, T_2$, $\hat{i}_z$ diverges from i_z.

In Figs. 23 and 24, the MMC rig operates under light load with a circulating current $I_z = I_{zo}/12 = 0.43$ A. According to (16), the observer gain and threshold value have been chosen as $L = 1500$, $I_{\text{th1}} = 5.2$ A, $I_{\text{th2}} = 2.6$ A (the black dash line). An open-circuit fault occurs at cell $5, T_1$ at 0.1 s. It can be seen that the open-circuit fault can be located in 50 ms.

Transient operation does not disturb the proposed FDI method. An experimental test is undertaken with modulation index of the ac voltage changes from 0.6 to 0.95 at 0.07 s and

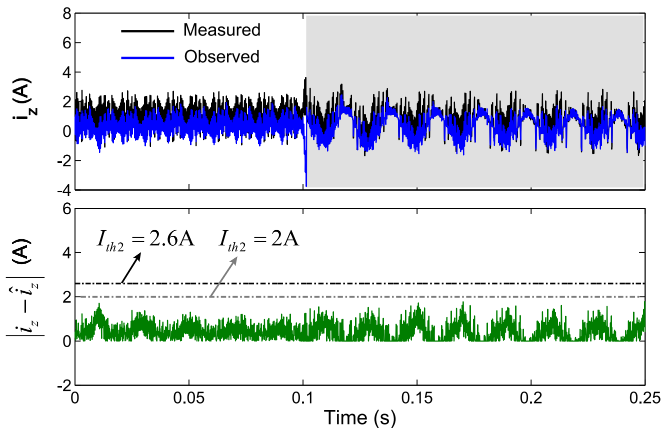

Fig. 23. Experimental results of the FDI under light load: open-circuit fault occurs at cell $5, T_1$ and the assumed faulty switch is cell $5, T_1$.

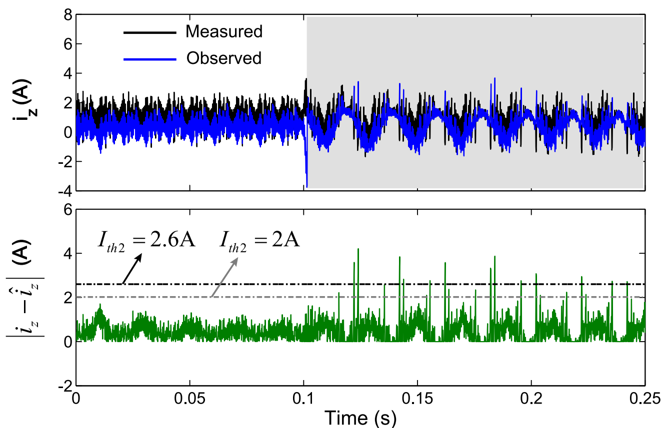

Fig. 24. Experimental results of the FDI under light load: open-circuit fault occurs at cell $5, T_1$, while the assumed faulty switch is cell $8, T_1$.

changes back at 0.12 s. The experimental results are shown in Fig. 25, where $\hat{i}_z$ follows i_z nicely regardless of the i_z fluctuation.

D. Discussion on the Detection Time

The choice of threshold value in an FD system such as the one we have described is always a compromise between the time for detection and the certainty of a correct detection. In the simulation and experimental results above, we have used a very conservative value for the threshold which yields a detection time of 50 ms. During this time, the capacitor voltage of the faulty cell in the 24-MW MMC rises to approximately 2300 V according to Fig. 1. While this is unlikely to be an issue for the semiconductors (usually rated at 3.3 kV), it might be unacceptable in terms of the headroom on capacitor voltage rating. In addition, careful coordination would be required with any local overvoltage protection. The detection time can be reduced by selecting a less conservative threshold as indicated in the results of Fig. 26 for the experimental rig, where an open-circuit fault occurs at cell $5, T_1$ at 0.05 s and is automatically detected and removed once located. Here, we have selected a threshold of

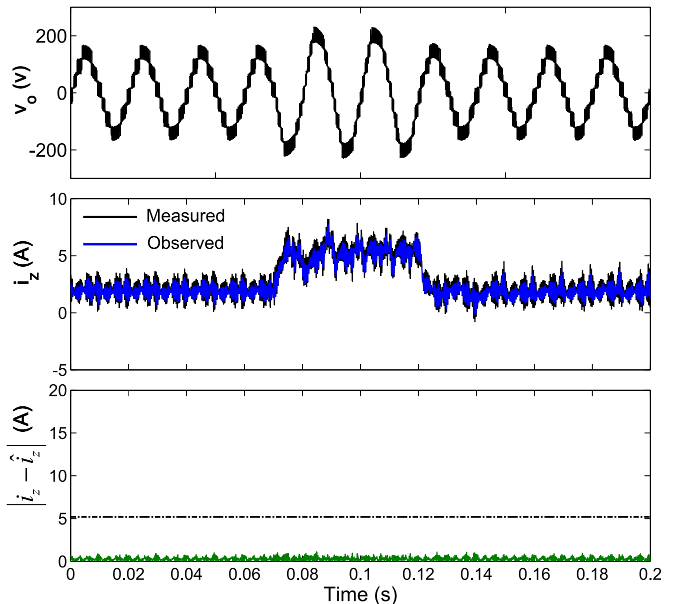

Fig. 25. Experimental results with changes in modulation index of the ac voltage.

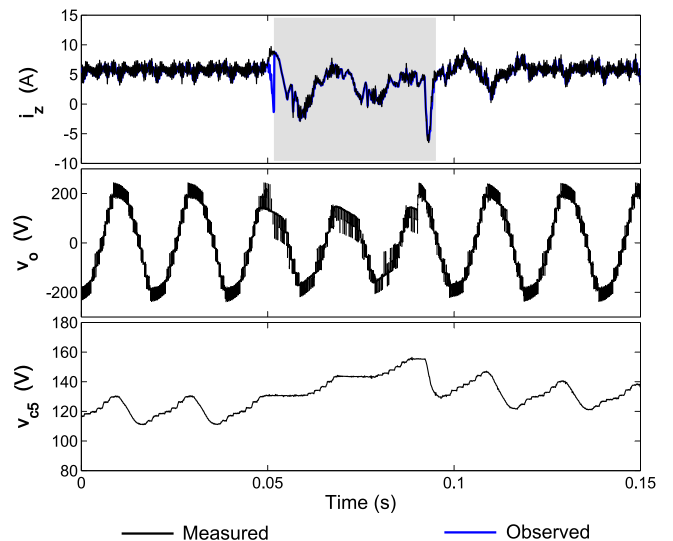

Fig. 26. Experimental results of the automatic FDI with smaller I_{th2}.

$I_{\mathrm{th2}} = 2$ A (indicated in Figs. 21–24), which still gives good certainty of FD and yields a detection time of 20 ms, reducing the impact on the capacitor voltages considerably. Clearly, the exact situation in a practical converter will differ from that in our laboratory prototype and selection of an appropriate threshold will be an important consideration.

VI. Conclusion

This paper has presented an SMO-based FDI technique applied to an MMC. The technique can detect and locate an open-circuit fault of a power semiconductor device or a gate driver failure in less than 50 ms. This method is simple with only one SMO equation and requires no additional transducers or circuits.

However, this method is not suitable for the detection and isolation of a short-circuit faulty device due to the very fast response requirement (10 μs). It is suggested that the proposed method works together with the hardware detection methods (for short-circuit fault) to achieve a more reliable MMC.

To improve the robustness of the FDI method, a technique is proposed to estimate parameter uncertainties, measurement errors, and other bounded disturbances, and the estimated value is used to compensate for the influence of the uncertainties and disturbances. As a result, the proposed technique can detect and locate an open-circuit faulty power semiconductor device while ignoring the parameter uncertainties, measurement noise, or other disturbances.

The FDI algorithm has been implemented in an FPGA using fixed-point arithmetic and has been tested on an experimental scaled-down, single-phase, eight-cell MMC converter. Experimental results have verified the analysis and simulation results. According to the experimental results, it is possible to use a smaller threshold value to detect and locate an open-circuit fault in less than 20 ms.

This FDI method can be applied to other converters with modular topologies employing similar analysis and principles. Furthermore, it is possible to apply this method for the detection and isolation of multiple open-circuit faults in an MMC, although it will take longer to find the faults as there are many possible fault scenarios to be assumed.

Acknowledgment

The authors would like to thank Prof. G. Asher from the University of Nottingham and Dr. C. Oates from Alstom Grid for their constructive suggestions regarding this work.

References

[1] M. Glinka and R. Marquardt, "A new ac/ac multilevel converter family," *IEEE Trans. Ind. Electron.*, vol. 52, no. 3, pp. 662–669, Jun. 2005.

[2] G. Adam, O. Anaya-Lara, G. Burt, D. Telford, B. Williams, and J. McDonald, "Modular multilevel inverter: Pulse width modulation and capacitor balancing technique," *IET Power Electron.*, vol. 3, no. 5, pp. 702–715, Sep. 2010.

[3] M. Perez, S. Bernet, J. Rodriguez, S. Kouro, and R. Lizana, "Circuit topologies, modelling, control schemes and applications of modular multilevel converters," *IEEE Trans. Power Electron.*, vol. 30, no. 1, pp. 4–17, Jan. 2015.

[4] F. Richardeau and T. Pham, "Reliability calculation of multilevel converters: Theory and applications," *IEEE Trans. Ind.*, vol. 60, no. 10, pp. 4225–4233, Oct. 2013.

[5] R. Patton, R. Clark, and P. Frank, *Fault Diagnosis in Dynamic Systems: Theory and Applications* (ser. Prentice-Hall international series in systems and control engineering). New York, NY, USA: Prentice-Hall, 1989.

[6] F. Caccavale and L. Villani, *Fault Diagnosis and Fault Tolerance for Mechatronic Systems: Recent Advances* (ser. Engineering online library). New York, NY, USA: Springer, 2003.

[7] M. Kinnaert, "Fault diagnosis based on analytical models for linear and nonlinear systems—A tutorial," in *Proc. 15th Int. Workshop Principles Diagnosis*, 2003, pp. 37–50.

[8] R. Chokhawala, J. Catt, and L. Kiraly, "A discussion on IGBT short-circuit behavior and fault protection schemes," *IEEE Trans. Ind. Appl.*, vol. 31, no. 2, pp. 256–263, Mar. 1995.

[9] Z. Wang, X. Shi, L. Tolbert, F. Wang, and B. Blalock, "A di/dt feedback-based active gate driver for smart switching and fast overcurrent protection of IGBT modules," *IEEE Trans. Power Electron.*, vol. 29, no. 7, pp. 3720–3732, Jul. 2014.

[10] L. Chen, F. Peng, and D. Cao, "A smart gate drive with self-diagnosis for power MOSFETs and IGBTs," in *Proc. 23rd Annu. IEEE Appl. Power Electron. Conf. Expo.*, Feb. 2008, pp. 1602–1607.

[11] C. Davidson, A. Lancaster, A. Totterdell, and C. Oates, "A 24 mW level voltage source converter demonstrator to evaluate different converter topologies," in *Proc. Cigre*, 2012, pp. 0–9.

[12] S. Yang, A. Bryant, P. Mawby, D. Xiang, L. Ran, and P. Tavner, "An industry-based survey of reliability in power electronic converters," *IEEE Trans. Ind. Appl.*, vol. 47, no. 3, pp. 1441–1451, May 2011.

[13] R. Wu, F. Blaabjerg, H. Wang, M. Liserre, and F. Iannuzzo, "Catastrophic failure and fault-tolerant design of IGBT power electronic converters—An overview," in *Proc. 39th Annu. Conf. IEEE Ind. Electron. Soc.*, Nov. 2013, pp. 507–513.

[14] F. Richardeau, P. Baudesson, and T. Meynard, "Failures-tolerance and remedial strategies of a PWM multicell inverter," *IEEE Trans. Power Electron.*, vol. 17, no. 6, pp. 905–912, Nov. 2002.

[15] P. Lezana, R. Aguilera, and J. Rodriguez, "Fault detection on multicell converter based on output voltage frequency analysis," *IEEE Trans. Ind. Electron.*, vol. 56, no. 6, pp. 2275–2283, Jun. 2009.

[16] A. Yazdani, H. Sepahvand, M. Crow, and M. Ferdowsi, "Fault detection and mitigation in multilevel converter STATCOMs," *IEEE Trans. Ind. Electron.*, vol. 58, no. 4, pp. 1307–1315, Apr. 2011.

[17] S. Khomfoi and L. Tolbert, "Fault diagnosis and reconfiguration for multilevel inverter drive using ai-based techniques," *IEEE Trans. Ind. Electron.*, vol. 54, no. 6, pp. 2954–2968, Dec. 2007.

[18] Y. Song and B. Wang, "Survey on reliability of power electronic systems," *IEEE Trans. Power Electron.*, vol. 28, no. 1, pp. 591–604, Jan. 2013.

[19] B. MIRAFZAL, "Survey of fault-tolerance techniques for three-phase voltage source inverters," *IEEE Trans. Ind. Electron.*, vol. 61, no. 10, pp. 5192–5202, Oct. 2014.

[20] S. Shao, P. Wheeler, J. Clare, and A. Watson, "Fault detection for modular multilevel converters based on sliding mode observer," *IEEE Trans. Power Electron.*, vol. 28, no. 11, pp. 4867–4872, 2013.

[21] S. Shao, P. Wheeler, J. Clare, and A. Watson, "Open-circuit fault detection and isolation for modular multilevel converter based on sliding mode observer," in *Proc. 15th Eur. Conf. Power Electron. Appl.*, 2013, pp. 1–9.

[22] Y. Shtessel, C. Edwards, L. Fridman, and A. Levant, *Sliding Mode Control and Observation* (ser. Control Engineering). New York, NY, USA: Springer, 2013.

[23] V. Utkin, J. Guldner, and J. Shi, *Sliding Mode Control in Electro-Mechanical Systems* (ser. Automation and Control Engineering). Boca Raton, FL, USA: CRC Press, 2009.

[24] V. Utkin, "Variable structure systems with sliding modes," *IEEE Trans. Autom. Control.*, vol. 22, no. 2, pp. 212–222, Apr. 1977.

[25] M. Vasiladiotis, "Analysis, implementation and experimental evaluation of control systems for a modular multilevel converter," Master's thesis, Royal Inst. Technol., Stockholm, Sweden, 2009.

[26] M. Almaleki, P. Wheeler, and J. Clare, "Sliding mode observer design for universal flexible power management (Uniflex-PM) structure," in *Proc. 34th Annu. Conf. IEEE Ind. Electron.*, Nov. 2008, pp. 3321–3326.

[27] K. Ilves, S. Norrga, L. Harnefors, and H.-P. Nee, "On energy storage requirements in modular multilevel converters," *IEEE Trans. Power Electron.*, vol. 29, no. 1, pp. 77–88, Jan. 2014.

[28] M. Hagiwara and H. Akagi, "Control and experiment of pulsewidth-modulated modular multilevel converters," *IEEE Trans. Power Electron.*, vol. 24, no. 7, pp. 1737–1746, Jul. 2009.

Shuai Shao received the B.Eng. degree from Zhejiang University, Hangzhou, China, in 2010, and the Ph.D. degree in electrical engineering for his work on fault detection for multilevel converter from the University of Nottingham, Nottingham, U.K., in 2015.

His research interests include fault detection, multilevel converters, and VSC-HVDC.

Alan J. Watson (S'03–M'08) received the M.Eng. (Hons.) degree in electronic engineering from the University of Nottingham, Nottingham, U.K., in 2004, and the Ph.D. degree in power electronics, also from the University of Nottingham.

In 2008, he became a Research Fellow in the Power Electronics Machines and Control Group, working on the UNIFLEX project (http://www.eee.nott.ac.uk/uniflex/). Since 2008, he has worked on several projects in the area of high-power electronics including high-power resonant converters, high-voltage power supplies, and multilevel converters for grid-connected applications such as HVDC and FACTS. In 2012, he was promoted to a Senior Research Fellow before becoming a Lecturer in high-power electronics in 2013. His research interests include the development and control of advanced high-power conversion topologies for industrial applications, future energy networks, and VSC-HVDC.

Jon C. Clare (M'90–SM'04) was born in Bristol, U.K., in 1957. He received the B.Sc. and Ph.D. degrees in electrical engineering from the University of Bristol, Bristol.

From 1984 to 1990, he was a Research Assistant and Lecturer with the University of Bristol, where he was involved in teaching and research on power electronic systems. Since 1990, he has been with the Power Electronics, Machines and Control Group, The University of Nottingham, Nottingham, U.K., where he is currently a Professor of power electronics. His research interests include power-electronic converters and modulation strategies, variable-speed-drive systems, and electromagnetic compatibility.

Pat W. Wheeler (SM'11) received the B.Eng. (Hons.) degree in, 1990, and the Ph.D. degree in electrical engineering for his work on matrix converters, in 1994, both from the University of Bristol, Bristol, U.K.

In 1993, he moved to the University of Nottingham, Nottingham, U.K., and worked as a Research Assistant in the Department of Electrical and Electronic Engineering. In 1996, he became a Lecturer in the Power Electronics, Machines and Control Group, The University of Nottingham. Since January 2008, he has been a Full Professor in the same research group. He has published 400 academic publications in leading international conferences and journals.

Dr. Wheeler is a Member at Large and Distinguished Lecturer of the IEEE Power Electronics Society.